Extreme Mechanics Letters 51 (2022) 101590

Contents lists available at ScienceDirect

Extreme Mechanics Letters

journal homepage: www.elsevier.com/locate/eml

Quantifying the hierarchy of structural and mechanical length scales in granular systems

Ghassan Shahin [a], Eric B. Herbold [b], Stephen A. Hall [c,d], Ryan C. Hurley [a,e,*]

[a] Hopkins Extreme Materials Institute, Johns Hopkins University, Baltimore, MD 21218, USA
[b] Atmospheric, Earth, & Energy Division, Lawrence Livermore National Laboratory, Livermore, CA, 94550, USA
[c] Division of Solid Mechanics, Lund 22100, Sweden
[d] Lund Institute of Advanced Neutron and X-ray Science, Lund 22370, Sweden
[e] Department of Mechanical Engineering, Johns Hopkins University, Baltimore, MD 21218, USA

ARTICLE INFO

Article history:
Received 21 October 2021
Received in revised form 8 December 2021
Accepted 10 December 2021
Available online 18 December 2021

Keywords:
Granular materials
Representative elementary volume
Theory of Geostatistics
X-ray tomography, X-ray diffraction
Micromechanics

ABSTRACT

Continuum modeling of granular media is made possible by the existence of a length scale at and above which grain-resolved properties can be meaningfully homogenized. Progress has been made in identifying such length scales relevant to local structural properties such as porosity. However, a systematic analysis of scales above which different mechanical properties can be homogenized has yet to emerge. Here, X-ray tomography and 3D X-ray diffraction data are examined to identify such length scales. The data was obtained *in-situ* in compressed granular materials with rigid and flexible confinement. The experimental data are supplemented with validated discrete element simulations which examine different system sizes and different boundary conditions. Our study reveals a hierarchy in the length scales of granular solids, with lengths governing structural variables being the shortest, lengths of stress variables being intermediate, and lengths of energy dissipation being the longest. All structural and mechanical length scales obey a power law based on the theory of Geostatistics, implying that the length scales can be found by analyzing samples significantly smaller than the length scales themselves. The length scales are also found to be sensitive to boundary conditions, implying that they are extrinsic features of granular media.

© 2021 Elsevier Ltd. All rights reserved.

1. Introduction

Granular materials react to deformation through complex interactions of kinematics [1,2] and force chains [3,4]. Despite these complexities, continuum mechanics is effectively employed to predict their macroscopic behaviors [5–7]. This is possible because of the existence of an length scale above which collective grain-resolved properties and processes can be meaningfully captured through homogenized, macroscopic variables [8,9]. This assumption of scale separation is captured through the existence of a representative volume element (RVE), a material volume that encompasses a sufficient number of material constituents such that it can be assigned a homogenized property representative of lower length scales [10–14]. The assumption of scale separation has led to marked advances in modeling and interpreting heterogeneous solids (a review is provided in [15]), including for polymers [16–18], metals [19], composites [20–22], alloys [23,24], concrete [25–27], geomaterials [28–31], ceramics [32], and even media with multi-physics [33–36].

In granular mechanics, identifying the RVE size has been a topic of extensive research. Research has focused on understanding the behaviors and predicting the effective properties of particle systems [37–42] and has expanded with the rise of homogenization methods for multi-scale analysis [39,43–52]. Prior research was based on micro-structural measurements (e.g., [53,54]) and numerical computations (e.g., [55,56]) with a focus primarily on structural properties such as porosity and grain size distribution. Prior studies suggest that the RVE size varies from one material to another and also depends on the property under consideration, with distinct sizes identified for geometrical and elastic properties [33,54,55]. Despite these intriguing findings, prior studies have several limitations. First, they are based on numerical idealizations [54,55] and focus on specific boundary conditions [55]. Second, the scale assessment in these studies is based on non-objective metrics, which may explain some contradictory findings [54,55]. Finally, RVE sizes for mechanical quantities such as stress and energy remain under-explored [33].

The present study provides an investigation into the length scales governing granular media. Our study is based primarily on a unique dataset that includes microstructural observations made through *in-situ* X-ray tomography and 3D X-ray diffraction [57]. These X-ray methods enabled characterization of the

* Corresponding author at: Hopkins Extreme Materials Institute, Johns Hopkins University, Baltimore, MD 21218, USA.
E-mail address: rhurley6@jhu.edu (R.C. Hurley).

https://doi.org/10.1016/j.eml.2021.101590
2352-4316/© 2021 Elsevier Ltd. All rights reserved.

kinematic (strain and motion), kinetic (stress), and combined energy fields arising during mechanical loading. We focus on addressing the scale question under quasi-static loading. High-rate loading may result in wave propagation with its own characteristic size (e.g., solitary waves which have a characteristic width of 5 grain diameters [58] and shock waves which have a characteristic size of several grain diameters [59–61]), but is excluded from our analysis. We focus on several structural and mechanical properties including volume fraction, fabric, stress, and energy dissipation. Experimental measurements and RVE sizes are used to validate a discrete element method (DEM) model that is employed to investigate the following questions: (1) Can RVE measurements conducted on small systems be used to compute length scales for larger systems? (2) Are RVE-sizes intrinsic (depending only on grain properties) or extrinsic (depending on boundary conditions) features of granular materials? We employ the theory of geostatistics [62] and makes use of its RVE definition: an observation volume that maintains stationary probability density functions when sampled across space. Geostatistics enables objective assessment of RVE sizes through correlation functions and a volume expansion method. Alternative methods for quantifying RVE sizes from 3D imaging have been advanced in other areas of materials science (e.g., [63]).

The remainder of this paper is organized as follows. Section 2 provides a summary of the theory of geostatistics. Section 3 describes the experimental data. Section 4 discusses the implementation of the theory of geostatistics for the RVE size determination. Section 5 presents numerical simulations based on DEM simulations that are used to demonstrate a power law for length scales and to examine the sensitivity of RVE sizes for boundary conditions. The paper concludes with a summary and discussion of the findings.

2. Geostatistics

The theory of geostatistics provides a method of assessing the spatial homogeneity of random processes [62,64]. The theory has been applied to solids to characterize spatial fluctuations of material properties [35,65,66] and to infer macroscopic quantities from microscopic observables [13]. Geostatistics aims to determine an RVE size, which is a volume size that guarantees regularity and reproducibility and is the length scale above which a property of interest can be homogenized. In this statistical approach, a material's properties are assumed to arise from an underlying random process [62,67]. The random process has to fulfill conditions of *stationarity* and *ergodicity* [68]. Stationarity implies that the statistics of the considered property are independent of sampling location. Ergodicity implies that the statistics of a process averaged over an infinite domain coincide with the statistics of sufficiently-large subdomain samples [62].

In ergodic systems, characteristic lengths can be evaluated through the relationship

$$A = \lim_{v \to \infty} v \, \mathrm{var}\{z(v)\}, \tag{1}$$

where v is the sampling size, $z(v)$ is the property of interest computed over the sample volume, $\mathrm{var}\{z(v)\}$ is the variance of $z(v)$ over all samples at size v, and A is a material constant associated with the length scale of fluctuation. Convergence of Eq. (1) requires that an increase of sample volume is balanced by a commensurate reduction of the variance. In this regard, it has been argued that the trends of variance evolution can be used to inspect homogeneity [64]. In particular, the decay of the variance in samples of different sizes can be expressed as a function of the volume through

$$\mathrm{var}\{z(v)\} = \frac{A}{v^b}, \tag{2}$$

where b indicates the rate of variance reduction as a function of the sampling size. Empirical studies show that statistically homogeneous media exhibit asymptotic decay of the variance characterized by $b \geq 1$ [64]. Heterogeneous media display a lower decay rate with $0 < b < 1$. These ideas have previously been applied in the studies of heterogeneous and multi-physics solids [10,35,66], tumor tissues (e.g. [69,70]), and image analysis [71].

The evolution of b in Eq. (2) as a function of v provides a basis for identifying the transition from statistical heterogeneity to statistical homogeneity. In the homogeneous regime, where the sample is large enough to be considered an RVE and $b \geq 1$, Eq. (2) provides an estimate of property variance at a given v. This methodology is applied to the experimental data discussed in the following section to characterize the RVE size for various structural, kinetic and kinematic variables.

3. Experiments

The experiments were conducted at the European Synchrotron Radiation Facility, beamline ID11, and are described in detail in [57]. Testing was performed on two samples of single-crystal ruby particles with diameters between 140 μm to 150 μm (Sandoz Fils SA), a mean particle diameter, D_{50}, of 145 μm, and uniform roughness below 0.008 μm. In the first specimen (A), particles were poured into a 1.5 mm inner-diameter aluminum cylinder and compressed between 1.5 mm diameter steel platens. This specimen was subjected to 13 successive quasi-static load steps, and the readings from the load cell are reported in Fig. 1. The sample was loaded in compression in steps 1–7, unloaded in steps 8–9, and reloaded in steps 10–13. In the second specimen (B), particles were assembled in a polymer sleeve submerged in a fluid-filled pressure cell, and compressed between 1.5 mm diameter steel platens. The sleeve provided more freedom for the particles to move laterally as compared to specimen A. Sample B was first subjected to three hydrostatic load steps, raising the pressure in the cell to 3 MPa through increments of 1 MPa. The sample was then loaded quasi-statically via axial compression in steps 5–14 with lateral pressure held constant at 3 MPa. The load cell reading relative to its value at the end of hydrostatic loading is reported versus load step in Fig. 1b. The stiffness of the polymer sleeve did not permit lateral stresses to decrease to a pressure of 3 MPa and instead constrained the granular sample, leading to higher lateral stresses. Experiment B featured global stress ratios similar to experiment A [57]. Experiment B, however, displayed distinct kinematics, as particles were permitted and observed to move significantly in lateral directions.

Between sample strain increments in each experiment, the loading platen displacement was fixed while *in-situ* X-ray computed tomography (CT) and 3D X-ray diffraction (3DXRD) measurements were made by rotating the specimen 180° and 360°, respectively. Transmission radiographs were used to reconstruct CT images with $(1.54)^3$ μm^3 per voxel at each load step. CT images were processed to segment grains and measure contact orientations and particle kinematics across load steps. Diffraction patterns were analyzed to identify particle strain tensors, orientations, and stress tensors using techniques described in [72]. CT and 3DXRD datasets were combined to quantify inter-particle forces and energy dissipation due to frictional slip and twist at each inter-particle contact, as described in [57] (also see [73,74]).

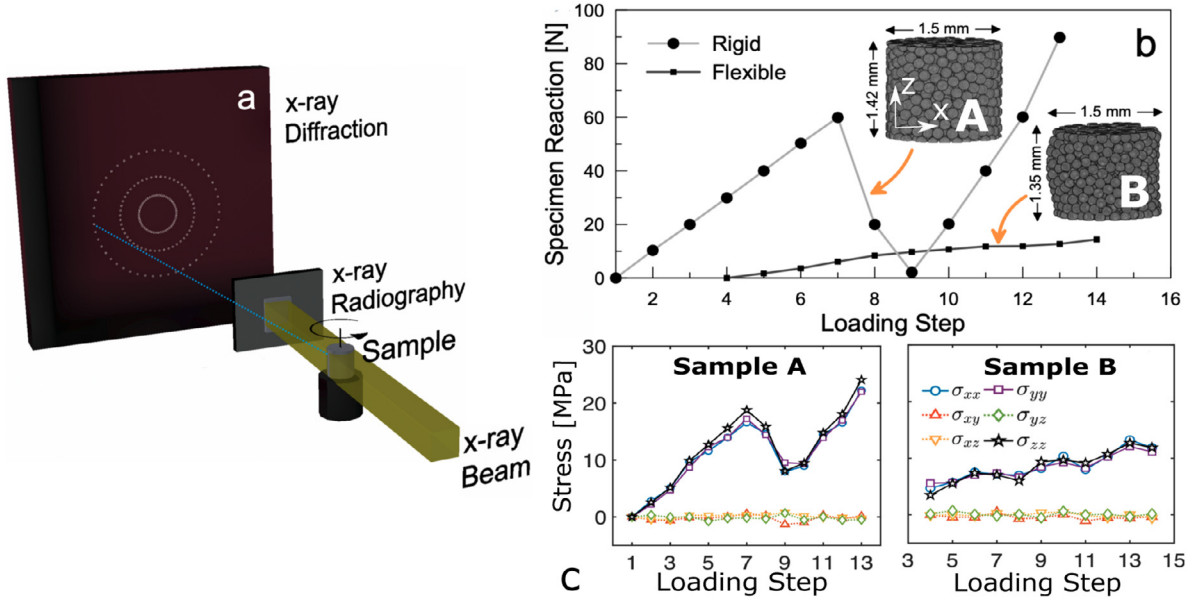

Fig. 1. (a) Schematic illustration of a synchrotron experiment with in-situ X-ray tomography and X-ray diffraction. (b) Load cell measurements from tests on granular systems with rigid and flexible confinement. Inset figures show CT images of the initial microstructure of the two samples. Each sample measures 1.5 mm in diameter. Initial sample heights are 1.42 mm (rigid confinement) and 1.35 mm (flexible confinement). (c) Homogenized grain-resolved stresses inferred from X-ray diffraction measurements in both samples.

4. Structural- and mechanical-property variograms

The methodology discussed in Section 2 is employed to characterize the RVE sizes associated with contact fabric, pore/grain volume fraction, mean and deviatoric stresses, mechanical fabric, and energy dissipation. From the stresses extracted from 3DXRD data, the mean, p, and deviatoric stresses, q, are computed for each particle as:

$$p = \frac{1}{3}\sigma_{ij}\delta_{ij}, \tag{3}$$

$$q = \sqrt{\frac{3}{2}s_{ij}s_{ij}}, \tag{4}$$

where σ_{ij} is the Cauchy stress tensor, δ_{ij} is Kronecker delta, and $s_{ij} = \sigma_{ij} - p\delta_{ij}$ is the deviatoric stress. From the forces and contact orientations extracted from CT and 3DXRD data, texture fabric, $\boldsymbol{F}$, and mechanical fabric, $\boldsymbol{F}_m$, are computed for a specific sampling volume as:

$$\boldsymbol{F} = \frac{1}{N}\sum_{i=1}^{N}\boldsymbol{n}\otimes\boldsymbol{n}, \tag{5}$$

and

$$\boldsymbol{F}_m = \frac{1}{N\langle F_n\rangle}\sum_{i=1}^{N}F_n\boldsymbol{n}\otimes\boldsymbol{n}, \tag{6}$$

where $\boldsymbol{n}$ is the contact normal vector at contact i, F_n is the normal force magnitude, $\langle F_n\rangle$ is the mean normal force magnitude over the sample, N is the number of contacts included in one sampling volume, and $\otimes$ is the dyadic tensor product (see [57] for information on how forces and normal vectors were calculated). The fabric tensors' deviators, computed analogously to Eq. (4) by replacing σ_{ij} by the fabric tensors, are used to calculate the variance evolution associated with the texture and the mechanical fabrics.

The elastic potential energy at contact i is calculated from the normal and tangential contact forces and kinematics as suggested in [57,75]:

$$E_n^i = \frac{4(3/4f_n)^{5/3}}{15(E^*)^{2/3}(R^*)^{1/3}}, \tag{7}$$

$$E_t^i = \frac{(f_t)^2(1+\nu)(2-\nu)}{8Ea}, \tag{8}$$

where f_n and f_t are the normal and tangential contact forces, $E^* = E/(2(1-\nu))$, E is Young's modulus, ν is Poisson ratio, and $1/R^* = 1/R_1 + 1/R_2$, with R_1 and R_2 being the contacting particles' radii computed as the spherical equivalent radius based on particle volume in CT images. E and ν are taken to be 350 MPa and 0.2, respectively, representative of the ruby particles used in experiments [57]. a is the contact radius that is equal to $\sqrt{R^*d}$, with d being the particle overlap quantified from the difference between the distance of contacting particles' centers and the sum of their radii.

All quantities (volume fraction, stress, fabric, and energy) are "rendered" onto distinct voxelized images with the same size as the segmented CT reconstructions for each load step of each experiment. For volume fraction, the voxelized images are binarized images in which particles are given a value of one and voids are given a value of zero. For mean and deviatoric stress, values for each grain are assigned to voxels belonging to the grains for which they are computed; voxels corresponding to voids are zero. For contact quantities including texture, mechanical fabric, and energy dissipation, a single voxel defining the associated contact point is assigned the value of the contact quantity; other voxels are zero.

Variograms portray the variance in a homogenized property as a function of sampling volume. To compute variograms for our data, we first tessellate the domain of interest within each rendered voxelized image into non-overlapping cubic subdomains of equal size. The homogenized property of interest in a subdomain is computed by averaging the value of all pixels, including voids, within that subdomain. The variance of homogenized properties across all subdomains is then calculated. The process is repeated for increasing subdomain sizes and the variance across all subdomains of a given volume is reported in the variograms. The reported variance is normalized by the point-variance for

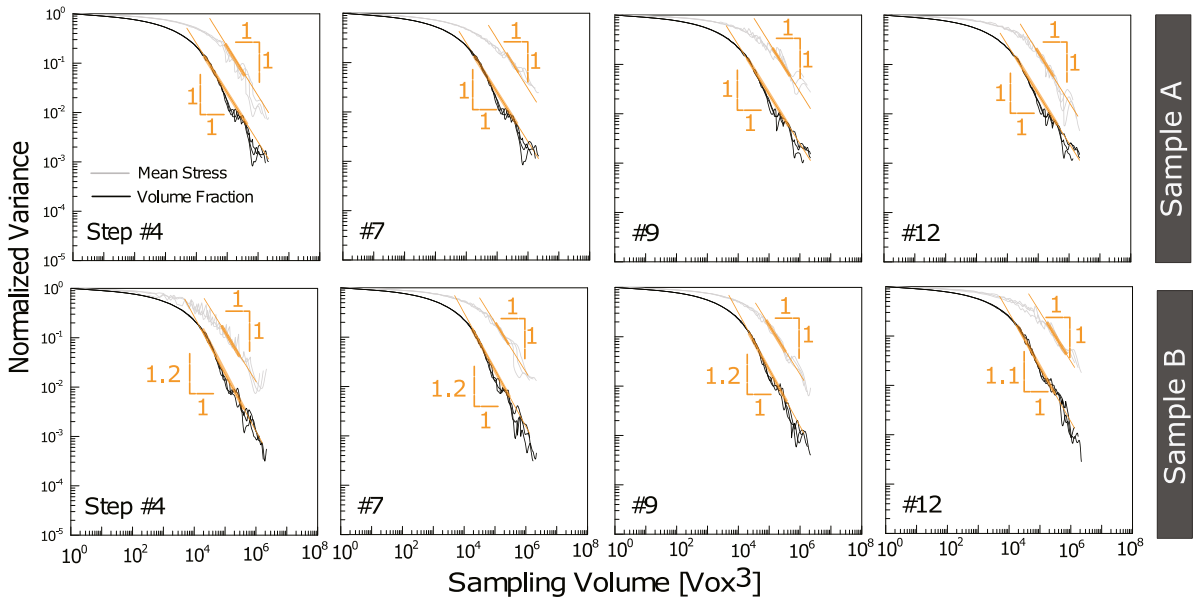

Fig. 2. Variograms of grain-volume fraction, f, and mean stress, p, computed for granular systems confined with (Upper, Sample A) rigid walls and (Lower, Sample B) flexible walls, displayed at selected loading steps. The variograms are normalized by the corresponding point-variance (the variance computed across all voxels in the "rendered" images described in the text). Variograms' asymptotes and their decay rate are illustrated. The variograms were computed for three domains of different sizes 260-, 240-, and 220-voxel (Appendix A).

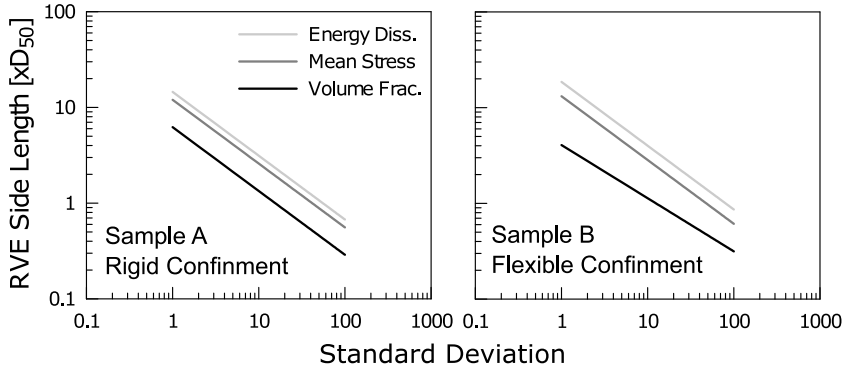

Fig. 3. RVE size as a function of the estimated standard deviation computed at step #6 for Sample A (left) and Sample B (right).

the property and domain of interest; the point-variance is the variance computed for all voxels in the "rendered" images.

Variogram analysis was conducted on a portion of the voxelized image created for each experimental sample at each load step. The portion of the images to be analyzed were identified as those in which the characteristics of the variance are not affected by the mechanical response at the boundaries (see Appendix A). The main sources of boundary-related heterogeneity in specimen A emerged only in regions near to the upper and lower boundaries. In specimen B, lateral boundaries also generated boundary-related heterogeneity. Statistical homogeneity was observed for a cubic portion of around 2/3 of the dimensions of each specimen. In the following, "specimen" indicates this isolated cubic domain in each sample.

A subset of variograms computed for solid volume fraction and mean stress by tessellating three cubic regions with sizes 260-, 240-, and 220-voxel side-length (see Appendix A), along with fits to their tails, are shown in Fig. 2. These variograms display a clear transition from slow to faster variance decay, with a decay exponent that is equal to or greater than one, indicating homogeneity.

4.1. Model-based interpretation of RVE size

Model fitting was carried out to identify the transition in b from values indicating statistical heterogeneity (i.e., $b < 1$) to those indicating statistical homogeneity (i.e., $b \geq 1$). Fitting was conducted by minimizing a mean squared error function:

$$MSE = \sum_{i=1}^{n} \left(var - \frac{A}{v^b} \right)^2 . \tag{9}$$

where var is the sampling variance. Optimization is performed in Matlab using the "fminsearch" function with b and A as optimization variables. A straightforward implementation of this strategy was systematically conducted for most variograms. Prior to calculating b using Eq. (9), variograms were smoothed through the Matlab function "smooth" which is based on weighted linear least squares and a second degree polynomial model, with a regression window of 30% of data points. Manual fitting, however, was necessary for variograms with stronger fluctuations that were not eliminated by this smoothing approach. Fluctuations in the tail of variograms emerge because of the decaying number

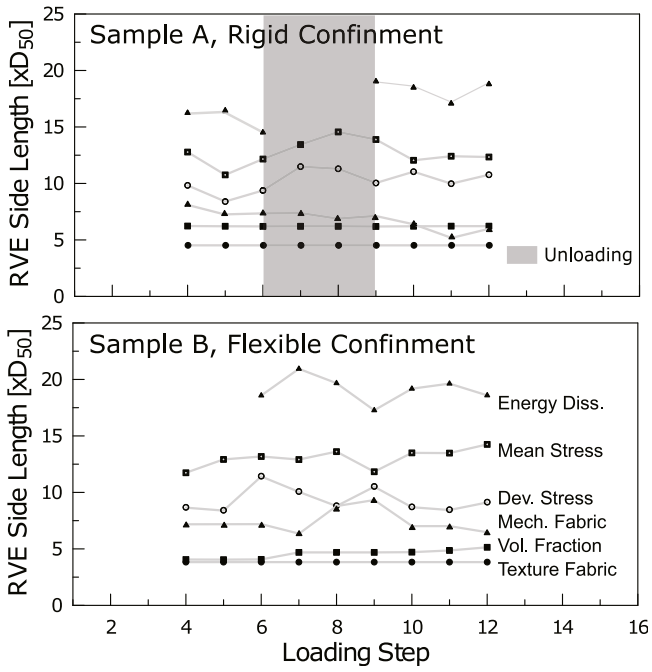

Fig. 4. RVE size evolution along loading computed for (from bottom to top) structural fabric, phase-volume fraction, mechanical fabric, deviator stress, mean stress, and energy dissipation. The volume is determined for a 1.0% standard deviation.

of sub-domains considered when v increases. Manual fitting was conducted by adjusting fitting parameters until the power-law curve visually aligned with the variogram tail (see Appendix B).

The relationship between the RVE size and the standard deviations of properties, as estimated using Eq. (2), is illustrated in Fig. 3 for load step 6 in both experiments. The standard deviation in this figure is the square root of the normalized variance shown in Fig. 2. The reported results include standard deviations calculated for volume fraction, mean stress, and energy dissipation using Eq. (2). We choose a standard deviation of 1% as our definition of an RVE size, although other standard deviations may be chosen with similar qualitative results. In Fig. 4, we report the 1% RVE sizes as multiples of D_{50}. Average RVE sizes across all load steps for each experiment are approximately 4, 5, 9, 10, 12, and 20 $\times D_{50}$ for structural fabric, volume fraction, mechanical fabric, deviatoric stress, mean stress, and energy dissipation, respectively. Both granular systems feature nearly constant RVE sizes throughout the experiments, even during the cycle of unloading–reloading executed on specimen A. Furthermore, despite differences in the lateral confinement of the two specimens, the characteristic lengths are comparable. These results suggest that characteristic lengths of granular systems are quantitatively ordered into a hierarchy, with structural properties (fabric, volume fraction) being the shortest, mechanical properties (mechanical fabric and stresses) being intermediate, and plastic properties (energy dissipation) being the longest. This finding was also discussed qualitatively in [57] using the exponents of exponential fits to probability distributions, but without providing quantitative RVE sizes.

5. Scale law and extrinsic effects

This section addresses two main questions: (1) Can RVE sizes be identified from samples smaller than the sizes themselves? (2) Are RVE sizes intrinsic properties, depending only on grain properties, or extrinsic properties, depending on grain properties and boundary conditions? DEM simulations with mechanical and statistical predictions validated against the experimental measurements discussed in the previous section are used to address these questions.

Table 1
Contact model used in DEM simulations.

Definition	Ruby	Quartz
Young's modulus [GPa]	350	70
Poisson Ratio	0.2	0.2
Particle–particle friction coefficient	0.25	0.2
Particle–wall friction coefficient	0.05	0.05
Restitution coefficient	0.7	0.7

5.1. DEM model and validation

DEM simulations of uniaxial, confined compression are performed in LIGGGHTS [76]. Four sample sizes are studied, but the sample used for validation against experimental data includes about 900 spherical particles. All samples are prepared in a cylindrical geometry with the cylinder axis aligned vertically. The experimental particle-to-cylinder diameter ratio is 1:10. The DEM simulations use bi-disperse particles with $\pm$ 10% diameter variation to avoid crystallization, similar to the grain size variation in experiments. The cylindrical walls have the same grain properties. Particles are generated randomly within the cylinder and then compressed to about 1 MPa by moving horizontal platen, having the same properties as the particles, downwards. Once compressed, each sample has a height to diameter ratio between 1 and 1.5, similar to experiments, and is then held at a fixed volume while kinetic energy is dissipated out of the system via damped particle motion.

The contact model includes linear-elastic, normal and tangential springs, with Coulomb type friction ("Hertz Tangential History" contact model [77]). Particles' elastic moduli and friction coefficients are taken to be representative of the ruby particles used in experiments. The model parameters are detailed in Table 1. Loading is applied by displacing a horizontal platen downwards at a strain rate of 10^{-5} until a desired nominal strain level is reached.

Statistical analysis, following the procedure discussed in previous sections, suggests that DEM simulations offer opportunities for further statistical analysis. The macroscopic response and characteristic lengths (volume fraction, stresses, energy), as well as their hierarchy, obtained from the DEM simulation with 900 particles are consistent with those characterized in the experiments, as shown in Fig. 5a–b. We note that our analysis also shows that the identified length scales are insensitive to elastic properties of the grains. To reduce the computational costs, the following analysis is therefore based on quartz-like, instead of ruby-like, properties (Table 1).

5.2. Scale power law

The focus of the following analysis is on examining the question of whether RVE sizes can be estimated in samples smaller than the sizes themselves by using power-law extrapolation. Variograms are generated for three simulation sizes, containing 2,000 (small), 20,000 (medium), and 40,000 (large) particles, and overlaid with one another to examine whether the decay of variance is similar in each case. The three simulation sizes, from smallest to

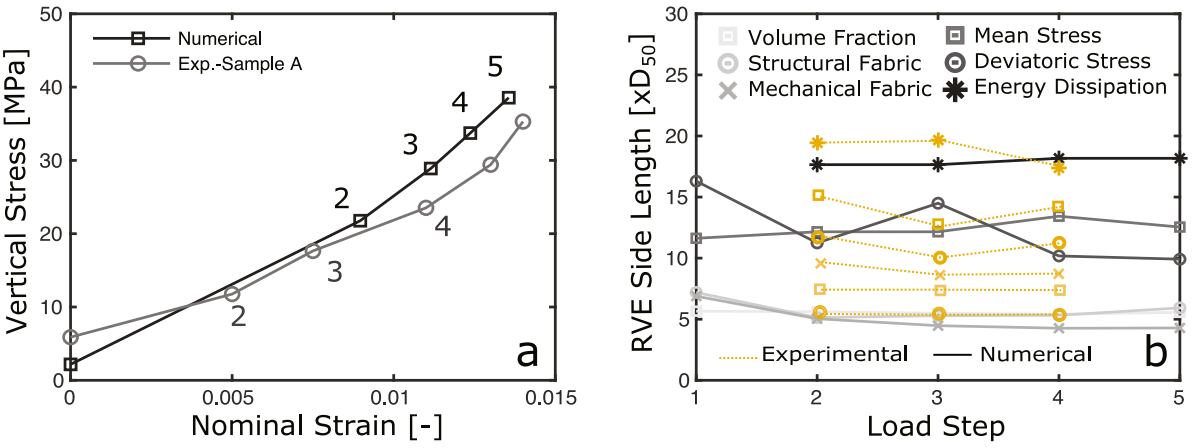

Fig. 5. Comparison of (a) macroscopic response and (b) characteristic lengths associated with 1% standard deviation between Sample A and a DEM simulation of the same uniaxial compression test, demonstrating accuracy at capturing characteristic lengths using DEM simulations.

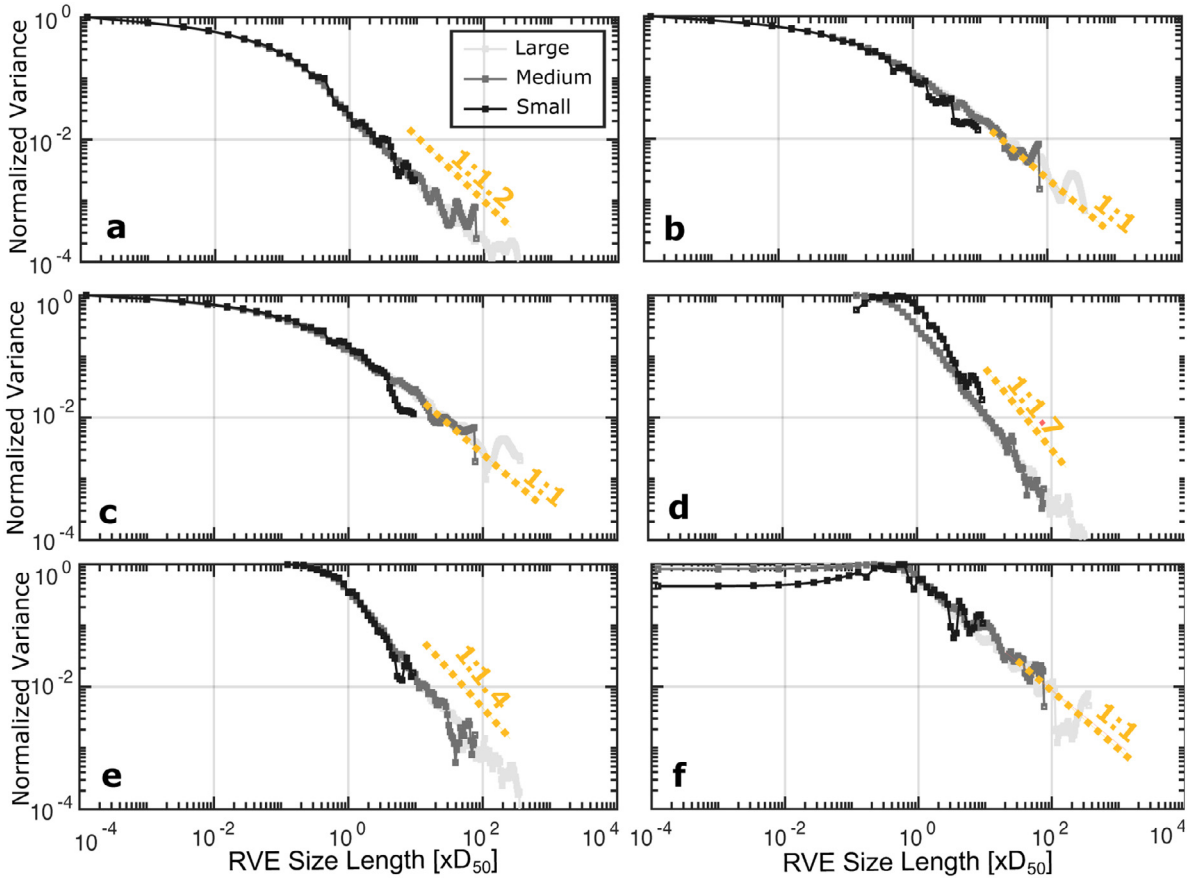

Fig. 6. Statistical analysis of structural and mechanical properties in granular systems with different sizes (described in the text) studied with DEM in cylindrical uniaxial strain geometry, showing that all variograms collapse into a single curve that obeys a power low. (a) Volume fraction, (b) mean stress, (c) deviatoric stress, (d) texture fabric, (e) mechanical fabric, and (f) energy dissipation.

largest, correspond to particle-to-cylinder diameter ratios of 1:10, 1:20, and 1:30, respectively. The specimens are subjected to uniaxial compression and analyzed following procedure discussed in Section 5.1.

The results of the RVE analysis based on DEM (Fig. 6) indicate that the tails of variograms for all sample sizes collapse onto a single curve. This suggests that homogeneous systems ($b \geq 1$) obey a power law that allows one to determine RVE sizes from samples smaller than the RVE size itself. One simply needs to use the power law obtained from analysis of variograms in the homogeneous regime ($b \geq 1$) to estimate the RVE size.

6. Length-scale sensitivity to extrinsic factors

This section focuses on the question of whether RVE hierarchy and sizes are intrinsic or extrinsic properties. DEM simulations of simple shear are employed for this purpose. The setup of the DEM simulation is shown in the inset to Fig. 7. The simple shear simulation is inspired by [78] and is based on a rectangular specimen with 40 D_{50} (length) $\times$ 20 D_{50}(width) $\times$ 20 D_{50} (height), and the same grain size and grain size distribution adopted in the simulations from Section 5.1. The simulation involves more than 12,000 particles. Periodic boundary conditions are imposed on the lateral sides. The upper and lower walls consist of rigidly connected particles with size and distribution similar to the system's bulk. The friction coefficient between the walls and particles is set to 0.9 to enhance surface friction [79]. Loading is conducted through the following protocol. The bottom wall is fixed in the vertical direction. The top wall is displaced downwards at a fixed rate until the vertical reaction stress between it and the particles has reached 10 MPa. This pressure is maintained throughout the simulations by treating the top wall as a rigid body and integrating its position in the same manner as particle positions are integrated, but by assuming the wall is subjected to a constant downward vertical force. Shearing is implemented by displacing, in opposite directions, the top and the bottom walls in the shear (length) direction, at a rate (defined as the relative shear velocity divided by the specimen height at the beginning of the shearing stage) of $\dot{\gamma} = 0.1$. The simulation is characterized by an inertial number, $I = \dot{\gamma}\, d_{50}/\sqrt{(P\rho)} \sim 10^{-6}$, where ρ is the material density. This value indicates quasi-static conditions [80].

Three deformation intervals are selected for RVE analysis (marked with circles in Fig. 7), in which the properties of volume fraction, mean stress, deviatoric stress, and energy dissipation are studied. Energy dissipation is studied for increments of about $\gamma = 0.01$. The selected intervals are located in the steady shearing stage, i.e., when deviatoric stress has reached a steady state. The analysis was conducted, as previously discussed, on subdomains to avoid boundary effects. The subdomains were identified by decreasing the investigated domain until homogeneity was consistently recovered (see for experimental data described in Appendix A). The subdomains covered almost the entire vertical dimension and 2/3 of the horizontal dimensions of the full simulation domain.

Results are illustrated in Fig. 8 along with the variograms of the first three steps in the simulations of uniaxial ("oedometric") compression with rigid walls, discussed in Section 5.1. Energy dissipation variograms for simple shear simulations suffered from poorly identified point-variance (variance when $v = 1$ voxel) because of strong fluctuations. The variograms were therefore normalized by the variance associated with a sampling volume of nearly 10 voxels, a size at which the variogram has displayed clearer trends. This shift does not affect variogram decay and has a minimal effect on the estimated RVE size.

The variograms in Fig. 8 display intriguing features. Although the variograms in both cases eventually display a variance decay as fast as or faster than the volume growth ($b \geq 1$), variograms associated with simple shear involve extended ranges of reduced decay ($b < 1$) for stresses and energy dissipation. Volume-fraction variograms are nearly the same in the uniaxial and shear cases. The differences in the variogram behavior indicate that simulated systems possess different kinetic and kinematic length scales depending on the boundary conditions. The dependency on boundary conditions suggests that the length scales are extrinsic properties of the material. Power-law fitting was conducted (Fig. 8) and the computed structural, kinetic, and kinematic RVE sizes for 1% standard deviation are reported in Fig. 9. The results reveal non-negligible increases in the stress and energy dissipation RVE-sizes for simple shear, as compared to uniaxial compression. Although the RVE sizes differ between the two loading conditions, the length-scale hierarchy is remarkably maintained. The structure-to-stress scale ratio doubled for the case of simple shear, while the stress-to-energy dissipation scale ratio appears to be comparable between the two loading conditions. This change may stem from the emergence of periodic, long force chains, which are known signatures of steady state simple shear flow in granular materials [81].

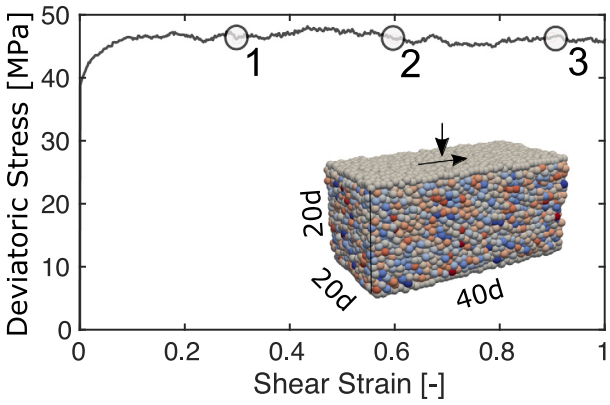

Fig. 7. Deviatoric stress response of a DEM simulation of simple shear test. Circles indicate three intervals of $\gamma = 0.01$ used for analysis. Colors in inset do not correspond particle properties.

7. Conclusions

The concept of a representative volume element or RVE, widely used in continuum-based idealizations of granular media, has been examined in this study. A range of structural, kinetic, and kinematic grain-scale properties were examined to identify the existence, size, and hierarchy of RVEs. The study is based on laboratory measurements of specimens compressed under various boundary conditions and monitored by combined X-ray tomography and the 3D X-ray diffraction. Specimens with rigid and moderately flexible lateral boundaries were considered. DEM simulations were also used to confirm that RVE sizes could meaningfully be extracted from systems smaller than the RVE size itself and that RVE sizes were extrinsic features of a system that depend on boundary conditions. The most significant findings of this study are:

1. RVE sizes have been quantified for contact fabric, pore/grain volume fraction, mean and deviatoric stresses, mechanical fabric, and energy dissipation.
2. RVE sizes follow a hierarchy: structural lengths associated with porosity and fabric are the shortest, kinetic lengths associated with stresses are intermediate, and kinematic (energy-dissipation) lengths are the longest.
3. The length scales obey power laws that can be obtained from systems smaller than the length scales themselves, as validated by DEM.
4. The RVE sizes are extrinsic properties of granular media, as granular systems under different boundary conditions displayed different kinetic and kinematic length scales. Despite the differences in amplitude, the hierarchy of the length scales appears to be maintained in different boundary conditions.
5. The length scales are state independent, as the RVE-sizes appear to be nearly invariable with the evolution of loading.

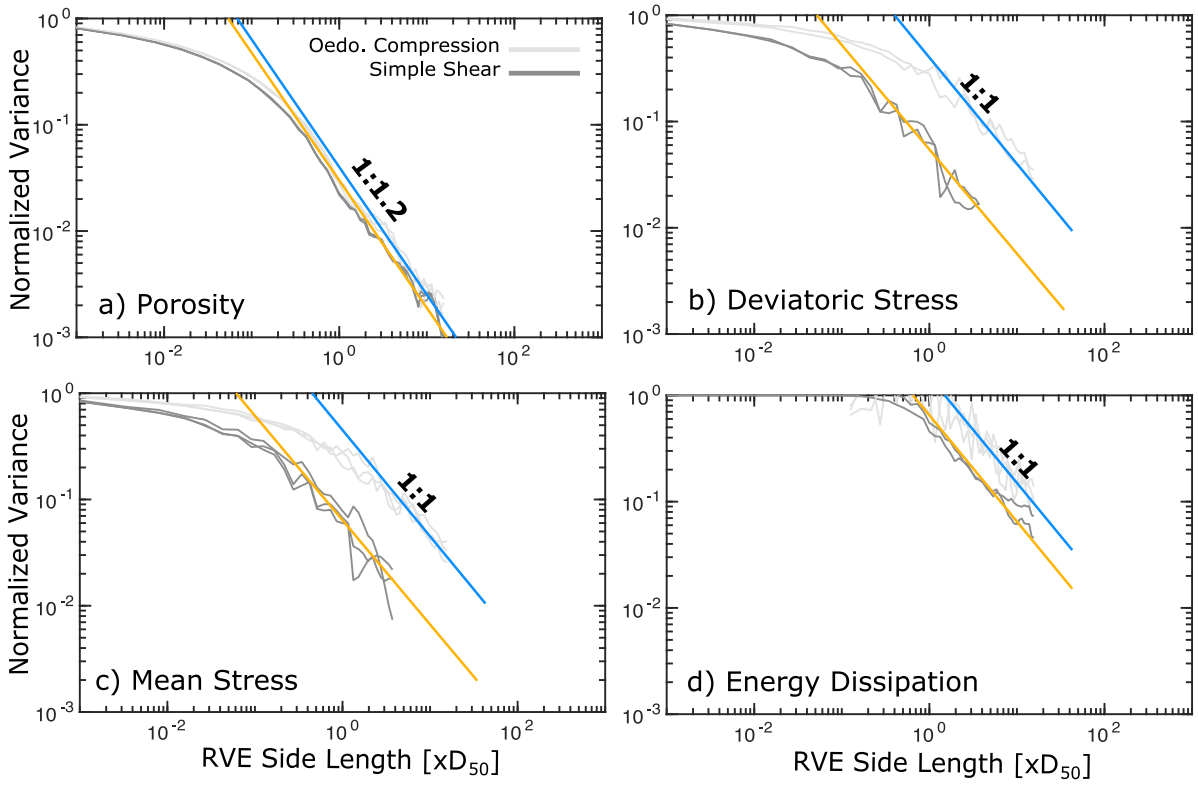

Fig. 8. Statistical analysis of structural and mechanical properties in granular systems with different boundary conditions, showing extrinsic characteristics of kinetic and kinematic length scales. The variograms correspond to three selected deformation intervals indicated by circles in Fig. 7.

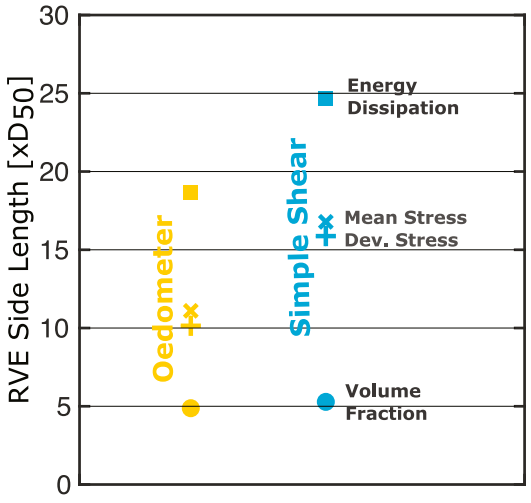

Fig. 9. RVE sizes associated with 1% standard deviation for uniaxial oedometric compression and simple shear simulations, revealing influences of boundary conditions on kinetic and kinematic length scales.

The findings of this research provide insight into the length scales dictating the constitutive properties of granular media. These findings support the development of microstructure- and mechanism-based constitutive models, as well as micro-to-macro homogenization methods. Our findings reveal that experiments performed on granular materials containing 10^3 grains are statistically valid for predicting structural and constitutive properties at much larger scales.

The identification of an RVE is conventionally constrained by two bounds: a lower bound at which the RVE is sufficiently large to represent homogenized behavior, and an upper bound set by field-scale spatial property fluctuations. Our analysis focused on the lower bound. Dedicated studies are needed to address the identification of the upper bound, primarily to support the integration of local heterogeneity in numerical analyses of spatial processes [82–84]. Our study quantified length scales under confined and unconfined uniaxial compression and simple shear. Triaxial compression under variable confining pressure should be performed in the future to help us understand any dependencies of the length scales on the stress state. Experiments involving cycles of loading–unloading and including variable deformation rates may be performed in the future to reveal any history- and rate-dependencies of the length scales. A small number of samples and small sample sizes were used in this study due to current experimental constraints. A larger number of samples and samples of a larger size should be used in future work to provide further validation and extension of the results presented here.

Declaration of competing interest

The authors declare that they have no known competing financial interests or personal relationships that could have appeared to influence the work reported in this paper.

Acknowledgment

The authors acknowledge the ESRF for synchrotron beam-time under proposal ma3373 and the helpful support of Dr. Marta Majkut and Dr. Jonathan Wright in experiment execution and Dr. Jonas Engqvist in load stage design. G.S. and R.C.H acknowledge support from the U.S. National Science Foundation CAREER Award No. CBET-1942096. Part of this work was performed under the auspices of the U.S. Department of Energy by Lawrence Livermore National Laboratory under Contract DE-AC52-07NA27344.

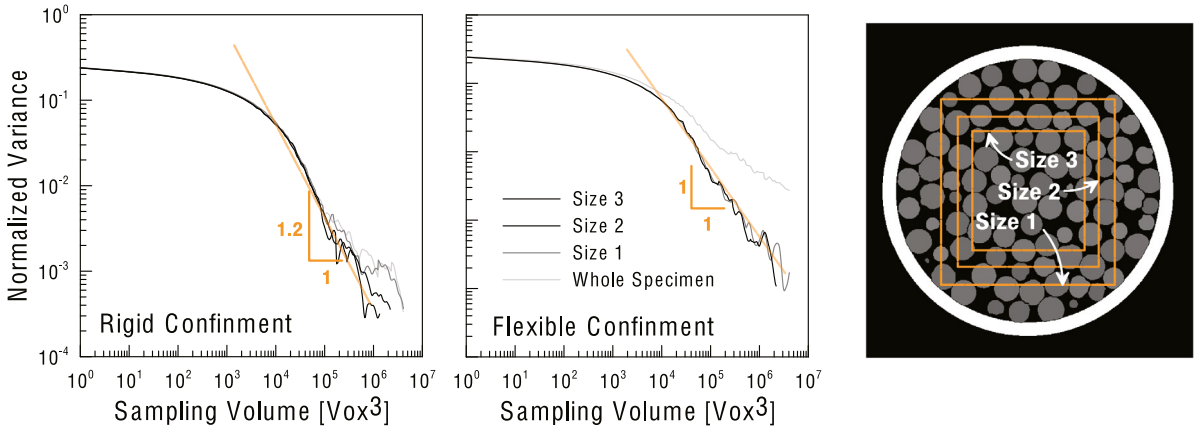

Fig. 10. Sensitivity analyses of analysis domain showing stability of variogram characteristics for a domain of interest with size equal to Size 2. The analysis presented here is for step #10.

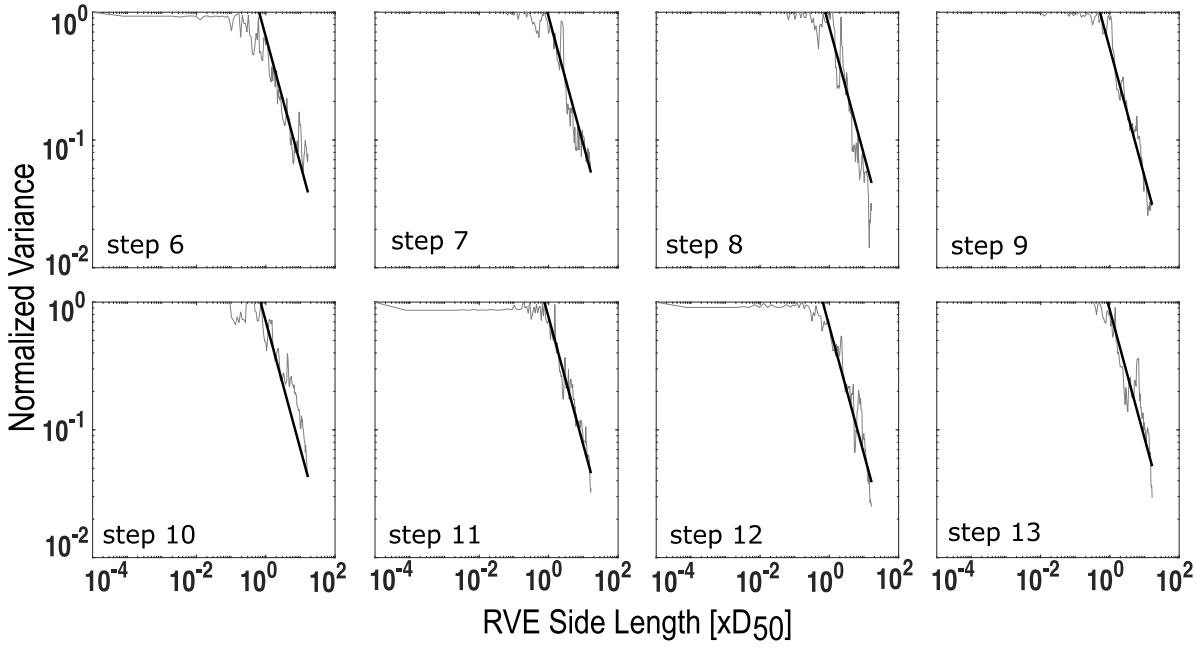

Fig. 11. Variograms of energy dissipation with manual fitting for the experimental triaxial compression. $b = 1$ in all cases.

Appendix A. Wall friction effects

Boundary effects generate heterogeneous kinematic and kinetic fields in the periphery of our granular specimens. Excluding this region from the analysis domain is necessary for material-based assessments of homogeneity and characteristic lengths that are insensitive to particle-boundary interactions. To identify this region, we examine cubic subdomains of with varying sizes centered at the mid-height of each specimen. For each cubic subdomain size, the statistical analysis discussed in the main text was applied by tessellating this domain. The domain of interest was identified as the largest subdomain size for which homogeneity is obtained in variograms of grain volume fraction. Fig. 10 illustrates the size of cubic subdomains with reference to a cross-section of sample A. The volume fraction variograms computed for subdomain sizes of 320- (Size 1), 260- (Size 2), and 220-voxels (Size 3) are reported in Fig. 10. In both experiments, the variogram characteristics are stable and do not feature heterogeneous tails as long the subdomain is Size 2 or smaller. This subdomain is used for analysis in the main text.

Appendix B. Variograms with manual fitting

This section illustrates a set of variograms for which fitting was conducted manually. Figs. 11, and 12, 13 show fitting conducted manually for energy dissipation variograms computed for experimental samples A, B, and the DEM simulation of rigidly-confined uniaxial compression, respectively. The case of step 7 and 8 are in Fig. 12 are associated with unloading steps and excluded from the analysis.

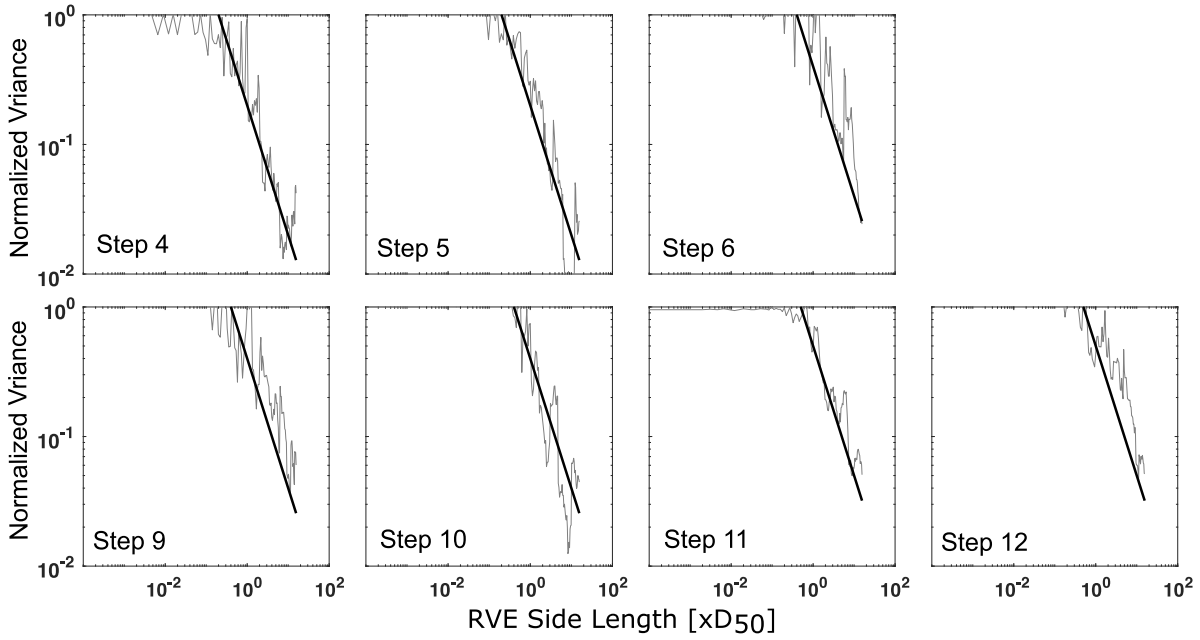

Fig. 12. Variograms of energy dissipation with manual fitting for the experimental uniaxial compression. $b = 1$ in all cases.

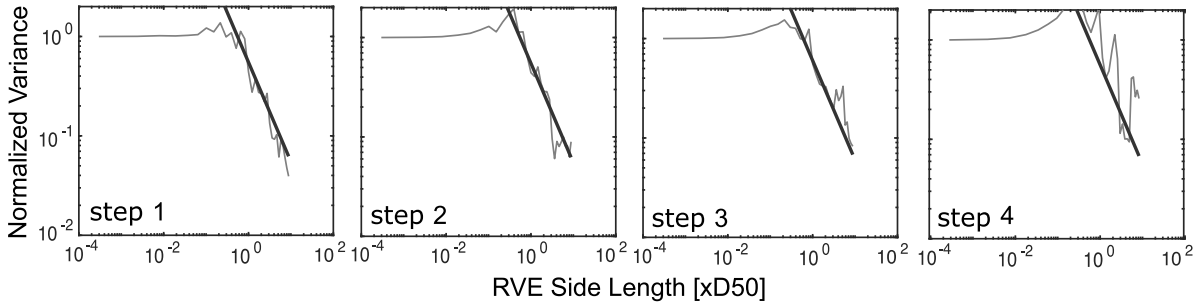

Fig. 13. Variograms of energy dissipation with manual fitting for uniaxial compression DEM simulation. $b = 1$ in all cases.

References

[1] F. Radjai, S. Roux, Turbulentlike fluctuations in quasistatic flow of granular media, Phys. Rev. Lett. 89 (6) (2002) 064302.

[2] J.F. Peters, L.E. Walizer, Patterned nonaffine motion in granular media, J. Eng. Mech. 139 (10) (2013) 1479–1490.

[3] F. Radjai, M. Jean, J.-J. Moreau, S. Roux, Force distributions in dense two-dimensional granular systems, Phys. Rev. Lett. 77 (2) (1996) 274.

[4] A. Tordesillas, G. Hunt, J. Shi, A characteristic length scale in confined elastic buckling of a force chain, Granul. Matter 13 (3) (2011) 215–218.

[5] Y. Forterre, O. Pouliquen, Flows of dense granular media, Annu. Rev. Fluid Mech. 40 (2008) 1–24.

[6] K. Kamrin, G. Koval, Nonlocal constitutive relation for steady granular flow, Phys. Rev. Lett. 108 (17) (2012) 178301.

[7] B. Andreotti, Y. Forterre, O. Pouliquen, Granular Media: Between Fluid and Solid, Cambridge University Press, 2013.

[8] R. Hill, Elastic properties of reinforced solids: some theoretical principles, J. Mech. Phys. Solids 11 (5) (1963) 357–372.

[9] W.J. Drugan, J.R. Willis, A micromechanics-based nonlocal constitutive equation and estimates of representative volume element size for elastic composites, J. Mech. Phys. Solids 44 (4) (1996) 497–524.

[10] T. Kanit, S. Forest, I. Galliet, V. Mounoury, D. Jeulin, Determination of the size of the representative volume element for random composites: statistical and numerical approach, Int. J. Solids Struct. 40 (13) (2003) 3647–3679.

[11] T. Kanit, F. N'Guyen, S. Forest, D. Jeulin, M. Reed, S. Singleton, Apparent and effective physical properties of heterogeneous materials: representativity of samples of two materials from food industry, Comput. Methods Appl. Mech. Engrg. 195 (33–36) (2006) 3960–3982.

[12] J. Desrues, R. Chambon, M. Mokni, F. Mazerolle, Void ratio evolution inside shear bands in triaxial sand specimens studied by computed tomography, GÉOtechnique 46 (3) (1996) 529–546.

[13] S.A. Hall, M. Bornert, J. Desrues, Y. Pannier, N. Lenoir, G. Viggiani, P. Bésuelle, Discrete and continuum analysis of localised deformation in sand using X-ray μCT and volumetric digital image correlation, GÉOtechnique 60 (5) (2010) 315–322.

[14] J.E. Andrade, I. Vlahinić, K.-W. Lim, A.X. Jerves, Multiscale 'tomography-to-simulation' framework for granular matter: the road ahead, GÉOtechnique Lett. 2 (3) (2012) 135–139.

[15] M. Ostoja-Starzewski, S. Kale, P. Karimi, A. Malyarenko, B. Raghavan, S. Ranganathan, J. Zhang, Scaling to RVE in random media, Adv. Appl. Mech. 49 (2016) 111–211.

[16] D. Trias, J. Costa, A. Turon, J. Hurtado, Determination of the critical size of a statistical representative volume element (SRVE) for carbon reinforced polymers, Acta Mater. 54 (13) (2006) 3471–3484.

[17] S. Mirkhalaf, F.A. Pires, R. Simoes, Determination of the size of the representative volume element (RVE) for the simulation of heterogeneous polymers at finite strains, Finite Elem. Anal. Des. 119 (2016) 30–44.

[18] W.M. Harris, W.K. Chiu, Determining the representative volume element size for three-dimensional microstructural material characterization. Part 1: Predictive models, J. Power Sources 282 (2015) 552–561.

[19] A. Borbely, H. Biermann, O. Hartmann, FE investigation of the effect of particle distribution on the uniaxial stress–strain behaviour of particulate reinforced metal-matrix composites, Mater. Sci. Eng. A 313 (1–2) (2001) 34–45.

[20] V. Bulsara, R. Talreja, J. Qu, Damage initiation under transverse loading of unidirectional composites with arbitrarily distributed fibers, Compos. Sci. Technol. 59 (5) (1999) 673–682.

[21] C. Pélissou, J. Baccou, Y. Monerie, F. Perales, Determination of the size of the representative volume element for random quasi-brittle composites, Int. J. Solids Struct. 46 (14–15) (2009) 2842–2855.

[22] P.K. Mohan, M.A. Kumar, P. Mohite, Representative volume element generation and its size determination for discontinuous composites made from chopped prepregs, Compos. Struct. 252 (2020) 112633.

[23] S. Graham, N. Yang, Representative volumes of materials based on microstructural statistics, Scr. Mater. 48 (3) (2003) 269–274.
[24] S. Yang, J. Dirrenberger, E. Monteiro, N. Ranc, Representative volume element size determination for viscoplastic properties in polycrystalline materials, Int. J. Solids Struct. 158 (2019) 210–219.
[25] I. Gitman, H. Askes, L. Sluys, Representative volume: Existence and size determination, Eng. Fract. Mech. 74 (16) (2007) 2518–2534.
[26] I. Gitman, M. Gitman, H. Askes, Quantification of stochastically stable representative volumes for random heterogeneous materials, Arch. Appl. Mech. 75 (2) (2006) 79–92.
[27] C. Zhou, K. Li, F. Ma, Numerical and statistical analysis of elastic modulus of concrete as a three-phase heterogeneous composite, Comput. Struct. 139 (2014) 33–42.
[28] O. Rozenbaum, S.R. du Roscoat, Representative elementary volume assessment of three-dimensional x-ray microtomography images of heterogeneous materials: Application to limestones, Phys. Rev. E 89 (5) (2014) 053304.
[29] B. Vik, E. Bastesen, A. Skauge, Evaluation of representative elementary volume for a vuggy carbonate rock—Part: Porosity, permeability, and dispersivity, J. Pet. Sci. Eng. 112 (2013) 36–47.
[30] J.O. Adeleye, L.T. Akanji, Pore-scale analyses of heterogeneity and representative elementary volume for unconventional shale rocks using statistical tools, J. Petrol. Explor. Prod. Technol. 8 (3) (2018) 753–765.
[31] A. Singh, K. Regenauer-Lieb, S.D. Walsh, R.T. Armstrong, J.J. van Griethuysen, P. Mostaghimi, On representative elementary volumes of grayscale micro-CT images of porous media, Geophys. Res. Lett. 47 (15) (2020) e2020GL088594.
[32] Z. Yan, S. Hara, Y. Kim, N. Shikazono, Homogeneity and representativeness analyses of solid oxide fuel cell cathode microstructures, Int. J. Hydrogen Energy 42 (51) (2017) 30166–30178.
[33] M.S. Costanza-Robinson, B.D. Estabrook, D.F. Fouhey, Representative elementary volume estimation for porosity, moisture saturation, and air-water interfacial areas in unsaturated porous media: Data quality implications, Water Resour. Res. 47 (7) (2011).
[34] J.-L. Auriault, C. Boutin, C. Geindreau, Homogenization of Coupled Phenomena in Heterogenous Media, Vol. 149, John Wiley & Sons, 2010.
[35] G. Shahin, M. Cil, G. Buscarnera, Assessment of statistical homogeneity in chemically treated granular materials, GÉOtechnique Lett. 8 (1) (2018) 32–39.
[36] X. Du, M. Ostoja-Starzewski, On the size of representative volume element for Darcy law in random media, Proc. Royal Soc. A 462 (2074) (2006) 2949–2963.
[37] L. Scholtès, B. Chareyre, F. Nicot, F. Darve, Micromechanics of granular materials with capillary effects, Internat. J. Engrg. Sci. 47 (1) (2009) 64–75.
[38] P.-Y. Hicher, C.S. Chang, Evaluation of two homogenization techniques for modeling the elastic behavior of granular materials, J. Eng. Mech. 131 (11) (2005) 1184–1194.
[39] C. Wellmann, C. Lillie, P. Wriggers, Homogenization of granular material modeled by a three-dimensional discrete element method, Comput. Geotech. 35 (3) (2008) 394–405.
[40] N.P. Kruyt, L. Rothenburg, Kinematic and static assumptions for homogenization in micromechanics of granular materials, Mech. Mater. 36 (12) (2004) 1157–1173.
[41] I. Goldhirsch, Stress, stress asymmetry and couple stress: from discrete particles to continuous fields, Granul. Matter 12 (3) (2010) 239–252.
[42] I. Agnolin, J.-N. Roux, Internal states of model isotropic granular packings. III. Elastic properties, Phys. Rev. E 76 (6) (2007) 061304.
[43] S. Ghosh, K. Lee, S. Moorthy, Two scale analysis of heterogeneous elastic-plastic materials with asymptotic homogenization and Voronoi cell finite element model, Comput. Methods Appl. Mech. Engrg. 132 (1–2) (1996) 63–116.
[44] F. Feyel, A multilevel finite element method (FE2) to describe the response of highly non-linear structures using generalized continua, Comput. Methods Appl. Mech. Engrg. 192 (28–30) (2003) 3233–3244.
[45] V. Kouznetsova, W. Brekelmans, F. Baaijens, An approach to micro-macro modeling of heterogeneous materials, Comput. Mech. 27 (1) (2001) 37–48.
[46] G. Shahin, J. Desrues, S.D. Pont, G. Combe, A. Argilaga, A study of the influence of REV variability in double-scale FEM× DEM analysis, Internat. J. Numer. Methods Engrg. 107 (10) (2016) 882–900.
[47] C. Miehe, J. Dettmar, D. Zäh, Homogenization and two-scale simulations of granular materials for different microstructural constraints, Internat. J. Numer. Methods Engrg. 83 (8–9) (2010) 1206–1236.
[48] M.G. Geers, V.G. Kouznetsova, W. Brekelmans, Multi-scale computational homogenization: Trends and challenges, J. Comput. Appl. Math. 234 (7) (2010) 2175–2182.
[49] N. Guo, J. Zhao, A coupled FEM/DEM approach for hierarchical multiscale modelling of granular media, Internat. J. Numer. Methods Engrg. 99 (11) (2014) 789–818.
[50] V.P. Nguyen, M. Stroeven, L.J. Sluys, Multiscale continuous and discontinuous modeling of heterogeneous materials: a review on recent developments, J. Multiscale Model. 3 (04) (2011) 229–270.
[51] J. Schröder, A numerical two-scale homogenization scheme: the FE 2-method, in: Plasticity and beyond, Springer, 2014, pp. 1–64.
[52] F. Larsson, K. Runesson, S. Saroukhani, R. Vafadari, Computational homogenization based on a weak format of micro-periodicity for RVE-problems, Comput. Methods Appl. Mech. Engrg. 200 (1–4) (2011) 11–26.
[53] M.R. Razavi, B. Muhunthan, O. Al Hattamleh, Representative elementary volume analysis of sands using X-ray computed tomography, Geotech. Test. J. 30 (3) (2007) 212–219.
[54] R. Al-Raoush, A. Papadopoulos, Representative elementary volume analysis of porous media using X-ray computed tomography, Powder Technol. 200 (1–2) (2010) 69–77.
[55] J. Wikacek, M. Molenda, Representative elementary volume analysis of polydisperse granular packings using discrete element method, Particuology 27 (2016) 88–94.
[56] M. Stroeven, H. Askes, L. Sluys, Numerical determination of representative volumes for granular materials, Comput. Methods Appl. Mech. Engrg. 193 (30–32) (2004) 3221–3238.
[57] C. Zhai, E. Herbold, S. Hall, R. Hurley, Particle rotations and energy dissipation during mechanical compression of granular materials, J. Mech. Phys. Solids 129 (2019) 19–38.
[58] V.F. Nesterenko, Propagation of nonlinear compression pulses in granular media, J. Appl. Mech. Tech. Phys. 24 (5) (1983) 733–743.
[59] V. Nesterenko, Dynamics of Heterogeneous Materials, Springer Science & Business Media, 2013.
[60] E. Herbold, V. Nesterenko, Shock wave structure in a strongly nonlinear lattice with viscous dissipation, Phys. Rev. E 75 (2) (2007) 021304.
[61] T. Vogler, M. Lee, D. Grady, Static and dynamic compaction of ceramic powders, Int. J. Solids Struct. 44 (2) (2007) 636–658.
[62] G. Matheron, Estimating and choosing. An essay on probability in practice, Springer-Verlag, 1989.
[63] M.P. Echlin, W.C. Lenthe, T.M. Pollock, Three-dimensional sampling of material structure for property modeling and design, Integr. Mater. Manuf. Innov. 3 (1) (2014) 278–291.
[64] C. Lantuéjoul, Ergodicity and integral range, J. Microsc. 161 (3) (1991) 387–403.
[65] C. Lantuéjoul, Geostatistical Simulation: Models and Algorithms, Springer Science & Business Media, 2013.
[66] J.-F. Bruchon, J.-M. Pereira, M. Vandamme, N. Lenoir, P. Delage, M. Bornert, X-ray microtomography characterisation of the changes in statistical homogeneity of an unsaturated sand during imbibition, GÉOtechnique Lett. 3 (2) (2013) 84–88.
[67] V. Howard, M. Reed, Unbiased Stereology: Three-Dimensional Measurement in Microscopy, Garland Science, 2004.
[68] L.M. Cruz-Orive, Stereology of single objects, J. Microsc. 186 (2) (1997) 93–107.
[69] V. Sharifi-Salamatian, A. de Roquancourt, J.P. Rigaut, Breast carcinoma, intratumour heterogeneity and histological grading, using geostatistics, Anal. Cell. Pathol. 20 (2, 3) (2000) 83–91.
[70] V. Sharifi-Salamatian, B. Pesquet-Popescu, J. Simony-Lafontaine, J. Rigaut, Index for spatial heterogeneity in breast cancer, J. Microsc. 216 (2) (2004) 110–122.
[71] R. Blanc, J.-P. Da Costa, Y. Stitou, P. Baylou, C. Germain, Assessment of texture stationarity using the asymptotic behavior of the empirical mean and variance, IEEE Trans. Image Process. 17 (9) (2008) 1481–1490.
[72] J. Oddershede, S.r. Schmidt, H.F. Poulsen, H.O. Sø rensen, J. Wright, W. Reimers, Determining grain resolved stresses in polycrystalline materials using three-dimensional X-ray diffraction, J. Appl. Crystallogr. 43 (3) (2010) 539–549.
[73] R. Hurley, S. Hall, J. Andrade, J. Wright, Quantifying interparticle forces and heterogeneity in 3D granular materials, Phys. Rev. Lett. 117 (9) (2016) 098005.
[74] M.R. Kuhn, K. Bagi, Contact rolling and deformation in granular media, Int. J. Solids Struct. 41 (21) (2004) 5793–5820.
[75] J. Zheng, A. Sun, Y. Wang, J. Zhang, Energy fluctuations in slowly sheared granular materials, Phys. Rev. Lett. 121 (24) (2018) 248001.
[76] C. Kloss, C. Goniva, A. Hager, S. Amberger, S. Pirker, Models, algorithms and validation for opensource DEM and CFD–DEM, Prog. Comput. Fluid Dyn. 12 (2–3) (2012) 140–152.
[77] CFDEM, LIGGGHTS v3.x documentation, 2020, URL https://www.cfdem.com/media/DEM/docu/gran_model_hertz.html.
[78] G. Ma, Y. Zou, K. Gao, J. Zhao, W. Zhou, Size polydispersity tunes slip avalanches of granular gouge, Geophys. Res. Lett. 47 (23) (2020) e2020GL090458.
[79] O. Dorostkar, R.A. Guyer, P.A. Johnson, C. Marone, J. Carmeliet, On the role of fluids in stick-slip dynamics of saturated granular fault gouge using a coupled computational fluid dynamics-discrete element approach, J. Geophys. Res. Solid Earth 122 (5) (2017) 3689–3700.
[80] GDR MiDi gdrmidi@ polytech. univ-mrs. fr http://www. lmgc. univ-montp2. fr/MIDI/, On dense granular flows, Eur. Phys. J. E 14 (2004) 341–365.

[81] F. Da Cruz, S. Emam, M. Prochnow, J.-N. Roux, F. Chevoir, Rheophysics of dense granular materials: Discrete simulation of plane shear flows, Phys. Rev. E 72 (2) (2005) 021309.
[82] R.I. Borja, X. Song, A.L. Rechenmacher, S. Abedi, W. Wu, Shear band in sand with spatially varying density, J. Mech. Phys. Solids 61 (1) (2013) 219–234.
[83] G. Shahin, G. Viggiani, G. Buscarnera, Simulating spatial heterogeneity through a CT-FE mapping scheme discloses boundary effects on emerging compaction bands, Int. J. Solids Struct. 206 (2020) 247–261.
[84] K. Karapiperis, M. Ortiz, J.E. Andrade, Data-driven nonlocal mechanics: Discovering the internal length scales of materials, Comput. Methods Appl. Mech. Engrg. 386 (2021) 114039.